# Impact of GHz and THz transport regimes on spin propagation and conversion in the antiferromagnet IrMn

O. Gueckstock, R. L. Seeger, T. S. Seifert, S. Auffret, S. Gambarelli, J. N. Kirchhof, K. I. Bolotin, Vincent Baltz, T. Kampfrath, L. Nádvorník

# Impact of GHz and THz transport regimes on spin propagation and conversion in the antiferromagnet IrMn

O. Gueckstock[1,2,**], R. Lopes Seeger[3,**], T. S. Seifert[1,2], S. Auffret[3], S. Gambarelli[4] , J. N. Kirchhof[1], K. I. Bolotin[1], V. Baltz[3*], T. Kampfrath[1,2], L. Nádvorník[5,*]

1. Department of Physics, Freie Universität Berlin, 14195 Berlin, Germany
2. Department of Physical Chemistry, Fritz Haber Institute of the Max Planck Society, 14195 Berlin, Germany
3. Univ. Grenoble Alpes, CNRS, CEA, Grenoble INP, IRIG-Spintec, F-38000 Grenoble, France
4. Univ. Grenoble Alpes, CNRS, CEA, SYMMES, F-38000 Grenoble, France
5. Faculty of Mathematics and Physics, Charles University, 121 16 Prague, Czech Republic

[*] E-mails: nadvornik@karlov.mff.cuni.cz, vincent.baltz@cea.fr

** contributed equally to this work

## Abstract

Control over spin transport in antiferromagnetic systems is essential for future spintronic applications with operational speeds extending to ultrafast time scales. Here, we study the transition from the gigahertz (GHz) to terahertz (THz) regime of spin transport and spin-to-charge current conversion (S2C) in the prototypical antiferromagnet IrMn by employing spin pumping and THz spectroscopy techniques. We reveal a factor of 4 shorter characteristic propagation lengths of the spin current at THz frequencies (~ 0.5 nm) as compared to the GHz regime (~ 2 nm) which may be attributed to the ballistic and diffusive nature of electronic spin transport, respectively. The conclusion is supported by an extraction of sub-picosecond temporal dynamics of the THz spin current. We also report on a significant impact of the S2C originating from the IrMn/non-magnetic metal interface which is much more pronounced in the THz regime and opens the door for optimization of the spin control at ultrafast time scales.

Antiferromagnetic spintronic devices[1] provide many advantages such as robustness against external magnetic fields, a higher memory bit integration, two orders of magnitude faster manipulation of the magnetic order and new topological phenomena[2, 3]. Their functionalities include pseudospin dynamics of magnons[4] and wide applications like memory[5-9], spin logic[10] and terahertz (THz) emission devices using pinning of a hard magnetic layer[11] or gradual reorientation of the Néel-vector[12]. To exploit these advantages, we need to control (i) the injection, (ii) transport and (iii) conversion of the spin angular momentum in antiferromagnetic materials.

A model metallic antiferromagnet (AFM) is IrMn in which spin-transfer effects[13], spin-orbit effects[14] and ferromagnetic reversal by spin Hall torques[15, 16] has been exploited. Regarding (i), an enhancement of the spin injection in IrMn by spin pumping around the Néel temperature at GHz frequencies may be possible[17]. In terms of (ii), in IrMn and structurally similar FeMn, two types of spin transport – electronic and magnonic – may exist at GHz frequencies[18, 19] as indicated by spin-pumping techniques. Experiments in FeMn[18] suggested different spin penetration depths in both regimes (1 and 9 nm). Lastly, regarding (iii), spin-to-charge-current conversion (S2C) in IrMn was studied at DC and AC frequencies, giving a spin Hall angle of a few percent[14, 20-22]. To utilize the full potential of antiferromagnetic spin transport, these features have to be transferred in the ultrafast regime that matches the dynamics of the antiferromagnetic order parameter. So far, only a few recent studies focused on the spin transport at terahertz (THz) frequencies[23-26].

In this paper, we explore the ultrafast (THz) spin injection, transport and S2C in $Ir_{20}Mn_{80}$ and directly compare them with transport experiments in the GHz range in equivalent samples. Our results indicate a change in the nature of the spin transport when transiting from the GHz to the THz regime. In addition, we show that the S2C is operative in IrMn at THz frequencies and reaches similar efficiencies as in the GHz range. Interestingly, we observe a strong influence of the IrMn/heavy-metal interface on the resulting in-plane charge current that is significantly more pronounced in the THz regime.

Our methodology is based on measuring the S2C of spin currents injected from a layer of ferromagnetic $Ni_{81}Fe_{19}$ (F) into a bilayer of IrMn (AF) and non-magnetic metal (N) [see Fig. 1(a),(b)]. Spin angular momentum is injected in two different frequency ranges by (i) ferromagnetic spin pumping at 9.6 GHz (defined by the ferromagnetic resonance of NiFe), using a continuous-wave electron paramagnetic resonance spectrometer fitted with a three-loop-two-gap resonator[27] [Fig.1(a)] and (ii) an ultrafast spin-voltage generation by an optical excitation pulse at 0.1-30 THz[28-30] (determined by its temporal duration) [Fig.1(b)]. In both techniques, the resulting out-of-plane spin current density $j_s(z)$ is converted to an in-plane charge current $I_c$ by the local spin Hall angle $\theta$ and generates a detectable electric field $E$, which is in the frequency domain given by

$$E(\omega) = Z(\omega) I_c(\omega) = eZ(\omega) \int j_s(z)\, \theta(z) dz \qquad (1)$$

Here, $z$ is the coordinate along the sample normal [see Fig. 1(a), (b)], $\omega$ is the angular frequency and $I_c(\omega)$ denotes the sheet charge current. $E(\omega)$ is detected (i) directly by electrical contacts with on sample, and (ii) contact-free by electro-optic sampling[31, 32] of the emitted THz pulse with a co-propagating probe pulse (0.6 nJ, 10 fs) in a 10µm-thick ZnTe(110) crystal under ambient conditions.

To investigate the propagation of $j_s(z)$ in both frequency regimes, we study thickness-dependent series of samples in the form of trilayers N|AF|F and F|AF|N. Each of them consists of a F = NiFe with thicknesses of 3 nm and 8 nm for THz and GHz experiments, respectively. The AF layer is $Ir_{20}Mn_{80}$ with varying thickness $d_{AF}$ ranging from 0 nm up to 12 nm with a paramagnetic-to-antiferromagnetic phase transition expected at $d_{AF} \approx 2.7$ nm at room temperature[17]. Finally, the sample structures contain a heavy metal layer with N = Pt, W or Ta (all 3 nm). All samples are deposited on thermally oxidized Si on glass substrates with

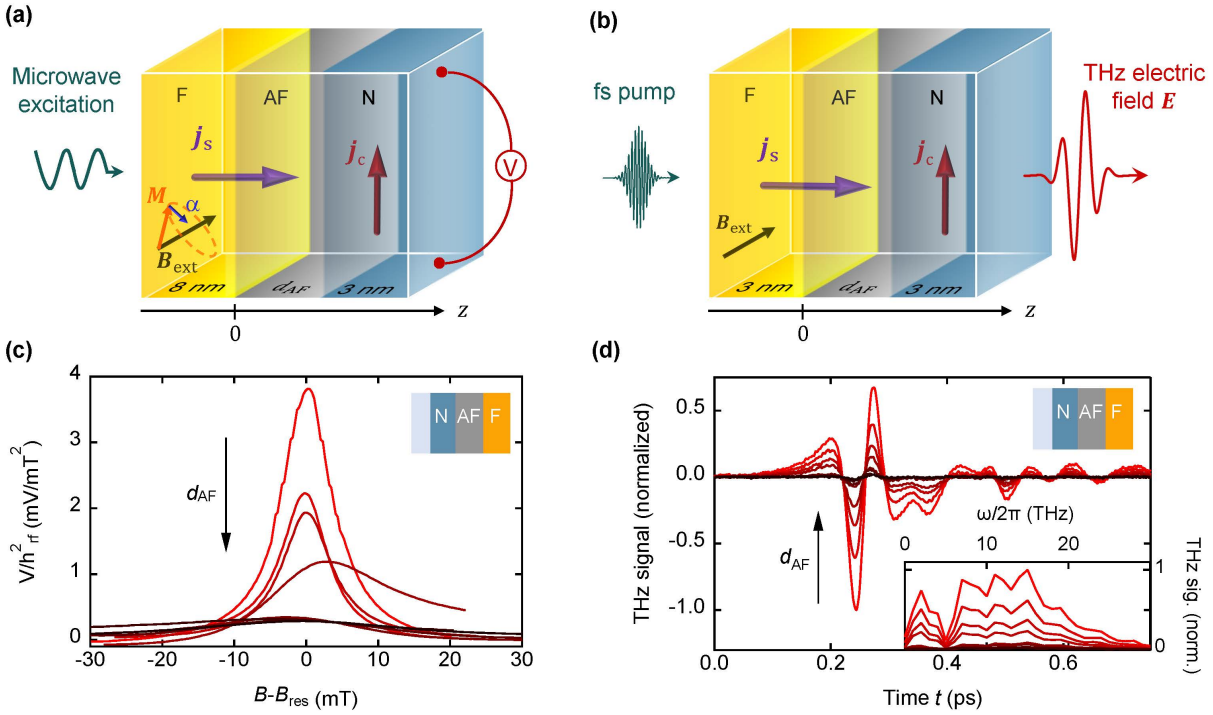


**FIG. 1. | Measuring inverse spin Hall effect at GHz and THz frequencies. (a)** Schematic of the GHz experiment. A microwave magnetic field (amplitude $h_{rf}$ ~ 0.05 mT, frequency 9.6 GHz) triggers the precession of magnetization in a magnetic layer (F = NiFe, thickness of 8 nm) and, due to spin pumping, launches a periodic spin current $\boldsymbol{j_s}$ through the antiferromagnetic layer IrMn (AF, thickness $\boldsymbol{d_{AF}}$) into a heavy metal layer (N, 3 nm) where it is converted into a detectable DC charge current $\boldsymbol{j_c}$ via the inverse spin Hall effect. **(b)** The analogous experiment performed at THz frequencies. A femtosecond optical pulse triggers an ultrafast $\boldsymbol{j_s}$ between the magnetic (F, 3 nm) and the AF layer. The converted $\boldsymbol{j_c}$ serves as a source of an emitted THz pulse. **(c, d)** Typical raw experimental data, illustrated here by N = Pt: normalized voltage $\boldsymbol{V/h_{rf}^2}$ in the GHz (c) and the electro-optical signal in the THz (d) experiments for different $\boldsymbol{d_{AF}}$ (black arrows indicate increase of $\boldsymbol{d_{AF}}$). All waveforms in (d) were normalized by the amplitude corresponding to $\boldsymbol{d_{AF} = 0}$. Inset: amplitude spectrum of the corresponding THz temporal waveforms.

thicknesses of Si(0.3mm)|$SiO_2$(500nm) and $SiO_2$(0.5mm) for GHz and THz experiments, respectively. A 2-nm-thick Al cap was deposited on all samples to form a protective AlOx film after oxidation in air. We note that the different thicknesses of the F layer serve to increase the impedance and, thus, increase the emitted THz amplitudes [Eq. (1)] or to reduce damping and subsequently increase spin injection efficiency in the spin pumping experiments[33, 34].

Typical raw signals from the GHz and THz experiment are shown in Fig. 1(c)-(d) for various values of $d_{\mathrm{AF}}$. In both experiments, the signal amplitudes decrease with increasing $d_{\mathrm{AF}}$. The bandwidth of the THz emission signal is large enough to capture sub-ps dynamics [Fig. 1(d) inset].

To separate the trivial $d_{\mathrm{AF}}$-dependent photonic and electronic effects, we normalize[35] the signals by independently measured $Z(\omega, d_{\mathrm{AF}})$ and absorbed power of the optical laser or electrical GHz excitation, and take the root-mean square. The raw GHz voltage [Fig. 1(c)] was further treated to obtain its symmetric component as described in Fig. S1 and Ref. [27]. The resulting signals, capturing the $d_{\mathrm{AF}}$-dependence of $I_{\mathrm{c}}$, which is a measure of the spin current $I_{\mathrm{S}}$ and S2C efficiency [Eq. (1)], are shown in Fig. 2. The underlying raw data sets are provided in Fig. S2. We also remove all method-specific impacts on the measured signal by normalizing the GHz and THz data sets to Pt|IrMn(0 nm)|NiFe at the respective frequency range.

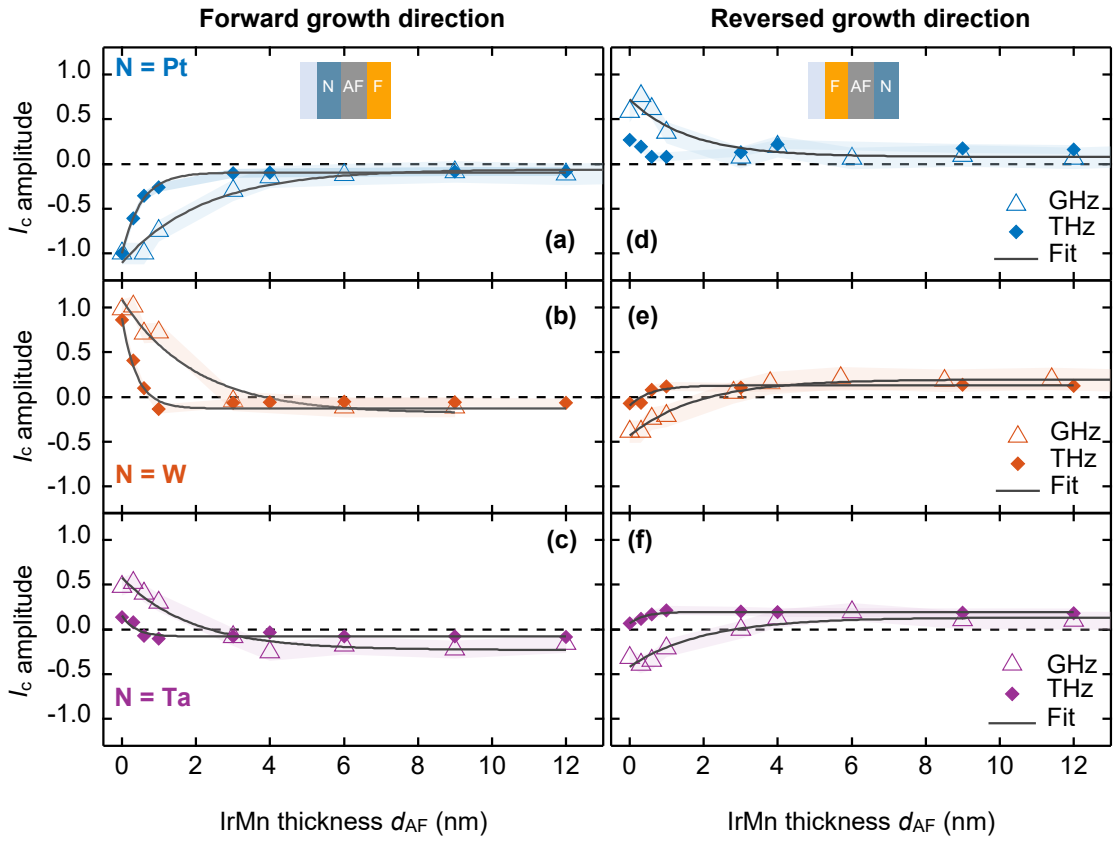


**FIG. 2. | Impact of IrMn thickness on GHz and THz charge current. (a)** Amplitude of charge currents $\boldsymbol{I_c}$ as a function of the IrMn thickness in N|IrMn|NiFe for N = Pt, **(b)** N = W and **(c)** N = Ta layer at both frequency ranges (GHz: open triangles, THz: closed diamonds). The data are normalized to $\boldsymbol{I_c}$ amplitudes obtained from Pt|IrMn($\boldsymbol{d_{AF}} = \mathbf{0}$)|NiFe in GHz and THz sets, resulting in the spin-to-charge current conversion (S2C) efficiency. **(d–f)** Same as (a–c), but for reversely grown NiFe|IrMn|N stacks. Photonic and electronic effects unrelated to the spin-to-charge conversion that vary with thickness are removed. Errors are comparable to symbol sizes. The color backgrounds are guides to the eye. Fits (gray curves) are vertically shifted mono-exponentials, giving the characteristic propagation lengths in IrMn. The fit values are summarized in Tab. 1.

We first analyze qualitatively the data in the "forward-grown" samples N|IrMn|NiFe [Fig. 2 (a)-(c)]. In both frequency regimes, we observe a change in the signal polarity for different N at $d_{\mathrm{AF}} = 0$, consistent with the sign and approximately the amplitudes of $\theta_{\mathrm{N}}$ known from literature ($\theta_{\mathrm{Pt}} > 0$ and $\theta_{\mathrm{W}}, \theta_{\mathrm{Ta}} < 0$)[36]. With increasing $d_{\mathrm{AF}}$, the signal decreases and, in the thick limit ($d_{\mathrm{AF}} > 5\ \mathrm{nm}$), saturates at approximately the same value for the THz and GHz experiments. The striking observation is the different rate of signal decay in both regimes which can be, in general, understood as a consequence of the finite propagation length of $j_{\mathrm{s}}(z)$.

We note that accurate modeling of $j_{\mathrm{s}}(z)$ in multilayers is typically complicated and requires determination of many unknown parameters such as spin mixing conductance of each interface[37]. For the sake of comparison of both regimes, we simplify the model by neglecting the back-reflections of $j_{\mathrm{s}}(z)$ and consider the IrMn layer a simple exponential spin-current attenuator[29]. Then, the total sheet charge current $I_{\mathrm{c}}$ from Eq. (1) can be separated to

$$I_{\mathrm{c}}(d_{\mathrm{AF}}) = I_{\mathrm{c,AF}} + I_{\mathrm{c,N}} + I_{\mathrm{c,a}} \approx \mathrm{I_{s,0}}\left[(\lambda\theta^*)_{\mathrm{AF}} + (\lambda\theta^*)_{\mathrm{N}} e^{-d_{\mathrm{AF}}/\lambda_{\mathrm{AF}}}\right] + I_{\mathrm{c,a}}. \qquad (2)$$

| | N | $\lambda_{\mathrm{IrMn}}$ (nm) at 0.5-30 THz | $\lambda_{\mathrm{IrMn}}$ (nm) at 9.6 GHz |
|---|---|---|---|
| **N \| IrMn \| NiFe (forward-grown)** | Pt | 0.6 ± 0.1 | 2.2 ± 0.5 |
| | W | 0.4 ± 0.1 | 2.0 ± 0.7 |
| | Ta | 0.4 ± 0.1 | 1.9 ± 0.5 |
| **NiFe \| IrMn \| N (reversed-grown)** | Pt | – | 1.6 ± 0.7 |
| | W | 0.5 ± 0.2 | 1.9 ± 0.3 |
| | Ta | 0.4 ± 0.1 | 2.0 ± 0.7 |

**TABLE 1. | Spin current characteristic lengths $\lambda$ as fitted from data shown in Fig. 2.** Fits are mono-exponential functions specified in the main text. The errors are obtained from fitting statistics and repeated experiments. The values of the other fit parameters $y_0$ and $y_1$ are summarized in the supplementary Tab. S1.

Here, $I_{\mathrm{s},0}$ is the total initial spin current launched by the excitation, $\lambda_i$ is the characteristic propagation length for the spin current in the corresponding layer $i = \mathrm{F}, \mathrm{AF}, \mathrm{N}$, and $\theta_i^*$ the effective spin Hall angle which includes all possible effects of spin memory loss and spin mixing conductance between the layers[38]. The last term $I_{\mathrm{c,a}} = I_{\mathrm{c,F}} + I_{\mathrm{c,I}}$ stands for an additional sheet charge current originating from S2C in the ferromagnetic layer and both interfaces[35]. Note that due to the simplifications, $\lambda_i$ cannot be rigorously taken as the spin-flip spin diffusion length but rather serves as a quantity to compare spin transport in both frequency regimes. Similarly, we can view the quantity $(\lambda\theta^*)_{\mathrm{i}}$ as the efficiency of the S2C that characterizes the practically achievable conversion in the layer including all mentioned spin injection losses.

We immediately see that the model explains well the data in Fig. 2(a)-(f). In the thin limit ($d_{AF} \lesssim \lambda_{\mathrm{AF}}$), the bulk S2C $(\lambda\theta^*)_{\mathrm{N}}$ is expected to dominate the S2C of the whole stack[14, 20-22] and the signal exponentially decreases with $d_{\mathrm{AF}}$. For the thick limit ($d_{\mathrm{AF}} > \lambda_{\mathrm{AF}}$), this contribution becomes negligible and the other, relatively small terms $I_{\mathrm{c,AF}}$ and $I_{\mathrm{c,a}}$ [Eq. (2)] can appear in the signal.

On a quantitative level, we use the model and fit the data in Fig. 2 by a mono-exponential function[29] $y(d_{\mathrm{AF}}) = y_1 \mathrm{e}^{-d_{\mathrm{AF}}/\lambda_{\mathrm{AF}}} + y_0$ where $y_1$ and $y_0$ stand for the relative conversion $(\lambda\theta^*)_N/(\lambda\theta^*)_{Pt}$ and the sum of all remaining relative S2C, respectively [Eq. (2)]. The obtained values are summarized in Tab. 1 and Tab. S1. We remind that the data shown in Fig. 2 are normalized to the signal from the Pt|NiFe reference sample in the respective frequency range. The average relative efficiency of the S2C for the thick limit $y_{0,\mathrm{THz}} \approx 8 \pm 1\%$ and $y_{0,\mathrm{GHz}} \approx 10 \pm 3\%$ in the THz and GHz regimes, respectively, are reaching consistently similar values. We can interpret the findings as a demonstration that the spin-current injection and propagation in IrMn is operative at ultrafast time-scales. In the thin thickness limit of IrMn, the layer behaves like a typical spin current attenuator in the ultrafast THz regime, qualitatively same as in the established GHz experiment[1, 39]. In the thick limit, when the ultrafast spin current does not reach the N layer, the role of the attenuator changes to a convertor and the THz S2C efficiency signals saturate at very close averaged values as in the reference GHz measurements. We note that we rule out another possible contribution to $I_{\mathrm{c}}$ originating from magnetic dipole radiation[30] as it is usually an order of magnitude smaller and we do not observe significant signals symmetric under sample reversal. Another source of the S2C signal may be the conversion in the F layer $I_{\mathrm{c,F}}$. Although this contribution is not always considered in the GHz experiments[1], we should take the observation of $y_0 \approx 8 - 10\%$ only as an estimate of the upper bound of $(\lambda\theta^*)_{\mathrm{IrMn}}/(\lambda\theta^*)_{\mathrm{Pt}}$, i.e., the practically achievable total conversion signal in IrMn relative to Pt.

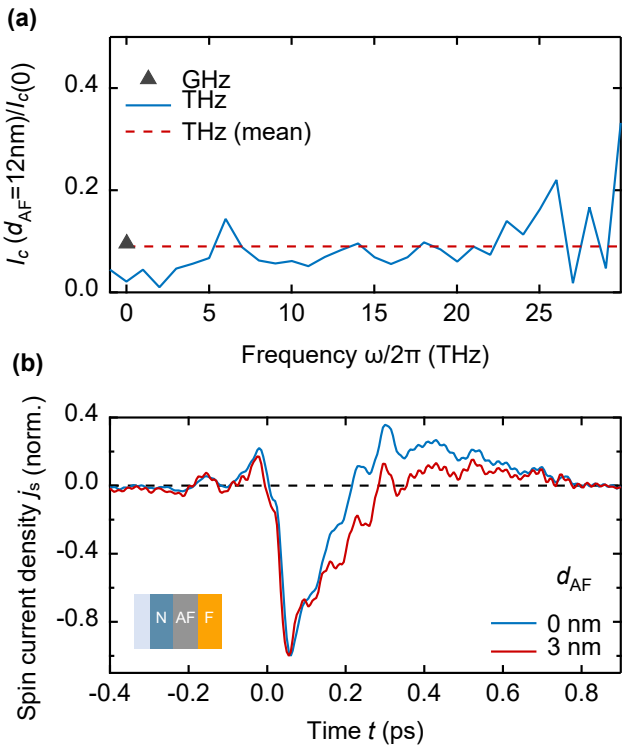


**FIG. 3. | Broadband THz charge current. (a)** Frequency dependence of the charge currents $\boldsymbol{I_c(d_{AF} = 12\,nm, \omega)/I_c(0, \omega)}$ for the thick limit normalized to the Pt|NiFe reference sample ($\boldsymbol{d_{AF} = 0}$). The data is extracted from the Pt|IrMn|NiFe series shown in panel Fig. 2 (a). The dotted red line depicts the mean value from the THz experiment corresponding to S2C in the thick limit (fitting parameter $\boldsymbol{y_{0,THz}}$, see Tab. S1). **(b)** Comparison of the THz spin current $\boldsymbol{j_s(t)}$ for $\boldsymbol{d_{AF} = 0}$ (blue curve) and 3 nm (red curve), both normalized to peak value $\boldsymbol{-1}$ for better comparability.

In addition to time-averaged values, the high temporal resolution of the THz experiment allows us to extract the $\omega$ dependence of $y_0$ taken from the THz data in Fig. 2(a). We observe flat response at 0.2-25 THz and approximately the same magnitude as the GHz value [Fig. 3(a)]. The good agreement of GHz and THz S2C efficiency in both thickness limits is consistent with previous studies that compared THz and low-frequency regimes of spin-orbit-coupling-based effects[29, 40, 41].

As $y_0 \ll y_1$ in most cases, the IrMn layer behaves like a spin current attenuator and we can justify the mono-exponential approximation in Eq. (2). Using the fitting values from Tab. 1, we obtain the mean $\lambda_{AF,THz} = 0.5 \pm 0.1$ nm and $\lambda_{AF,GHz} = 1.9 \pm 0.6$ nm, averaged over stacks with different N. We note that, except of the THz data in Fig. 2(d), we do not observe any significant irregularities in the GHz and THz signals around the ordering thickness at $d_{AF} \approx 2.7$ nm at room temperature.

Interestingly, the factor of 4 between $\lambda_{AF,THz}$ and $\lambda_{AF,GHz}$ may indicate a different regime of spin transport. To test this hypothesis, we extract the ultrafast dynamics of $j_s(t)$ from the THz signals from Pt|NiFe [blue curve in Fig. 3(b)] and Pt|IrMn(3 nm)|NiFe (red curve), where the IrMn is already antiferromagnetically ordered. More data are available in Fig. S3. Consistently to result in Fig. 2, we do not observe any clear and systematic change in the spin-current dynamics below and above the ordering thickness of IrMn. Moreover, in both samples, $j_s(t)$ follows very similar dynamics as reported in previous works on bilayer stacks[28, 30] consisting of standard metallic ferromagnets and the non-magnetic spin Hall material Pt[30]: a sharp rise followed by a decay on a time scale of 100 fs. Prior theoretical work[42] suggests similar dynamics

for electronic spin transport with relevant λ determined by the mean free path. This is in a sharp contrast to the magnonic spin transport reported in THz experiments[43, 44], showing a 1-ps-long dynamics.

Therefore, we can partly interpret the characteristic lengths $\lambda_{\mathrm{AF}}$, that differ by a factor of 4 between the THz and GHz data, as a consequence of different regimes of the electronic spin transport: The ballistic regime at the THz frequencies where the electronic mean free path is the relevant quantity[28, 30], and the diffusive regime at the GHz frequencies characterized by the electron spin diffusion (spin-flip) length[1]. Another contribution to the different $\lambda_{\mathrm{AF}}$ can be a possible mixture of the magnonic contribution[14, 18, 19, 45] in the GHz spin transport.

Finally, we focus on the reversely grown samples [Fig. 2 (d–f)]. If each stack NiFe|IrMn|Pt [Fig. 2 (d–f)] is a mirror image of its forward-grown partner Pt|IrMn|NiFe [Fig. 2 (a–c)], we would expect perfectly reversed signals since the spin and, thus, charge current flow is opposite and dominates over other THz-emission sources such as magnetic dipole radiation[30, 46, 47]. Any deviations from this behavior indicate deviations from the ideal mirror image, which can in particular arise from the interface[29, 48] and its quality[35]. Although these samples provide very consistent values of $\lambda_{\mathrm{AF}}$ and $y_0$ with the forward-grown stacks [Fig. 2 (a–c)], we do observe a significant change of signal amplitudes for thin AFM layers ($d_{\mathrm{AF}} < 2\ \mathrm{nm}$) quantified by $y_1 + y_0$ (Tab. S1). For instance, by comparing Fig. 2(b) and Fig. 2(e), the GHz data show a reduction of 2.5 (and smaller in other pairs), whereas the THz data differ by more than a factor of 9.

Moreover, the THz data from reversely grown samples not only differ in larger factors from their forward-grown counterparts, but can also follow a non-monotonic trend, e.g. in the Pt-based samples [Fig. 2(d) and Fig. S4]. Here, we compare the reversely grown Pt-series to a linear combination of signals from NiFe|IrMn and Pt|IrMn|NiFe that can reasonably reproduce the non-monotonic trend, indicating that the role of interfaces changed their weights as detailed in the supplementary material. Another striking signature of the interface impact manifests in reversely grown Ta-based samples [Fig. 2(f)] in which no polarity switching with increasing $d_{\mathrm{AF}}$ is observed at the thin limit. Such observation is unexpected considering the typical magnitude of the S2C conversion in Ta ($\theta_{\mathrm{Ta}} \approx 7\%$ [36]).

The dramatic reduction of the S2C amplitude, the non-monotonic $d_{\mathrm{AF}}$-dependence or even the change of polarity of the S2C in the thin limit of the reversed-grown series, represented by $I_{\mathrm{c,a}}$, can be understood in terms of the spin memory loss (represented by a finite size layer with spin-dependent spin-flip scattering such as a finite spin diffusion length) and spin asymmetry (represented by an infinitesimally thin layer with spin-dependent electronic scattering, i.e. with spin-dependent mean free path) introduced by one of the IrMn interfaces, as argued in Refs. [38, 49, 50]. The intrinsic nature of the above two processes is very different and may impact the THz and GHz experiments differently, considering their distinct $\lambda_{\mathrm{AF}}$. Since the variations of $I_{\mathrm{c,a}}$ due different N materials are much smaller in the thick limit than in the thin limit, we conclude that the more relevant interface is IrMn/N.

In conclusion, we have shown that the ultrafast spin injection and conversion in IrMn is operative up to ~25 THz and only limited by the pump pulse duration and detection bandwidth. The upper bound of the spin-to-charge conversion efficiency in IrMn, $(\lambda\theta^*)_{\mathrm{IrMn}}$, amounts to roughly 10% of the conversion in Pt. The direct comparison of the THz to GHz regimes revealed that the characteristic length of the spin transport is 4 times larger at the GHz frequencies. As underlying mechanism, we suggest the dominance of diffusive and ballistic electron transport in GHz and THz regimes, respectively. We also showed that the contribution of the IrMn/N interface to the spin-to-charge conversion can be significant and even dominate the other conversion processes, thus making it useful in optimizing and engineering the ultrafast spintronic functionalities in antiferromagnets.

See the supplementary material for further details on the experiments.

## Acknowledgments

The authors acknowledge funding by the collaborative research center SFB TRR 227 “Ultrafast spin dynamics” (projects B02 and A05), the ERC H2020 through projects CoG TERAMAG/Grant No. 681917, the French national research agency (ANR) [Grant Number ANR-15-CE24-0015-01], the CEA’s bottom-up exploratory program (Grant Number PE-18P31-ELSA) and the Czech Science Foundation (GA CR, Grant Number 21-28876J).

## Data availability

The data that support the findings of this study are available from the corresponding author upon reasonable request.

## Conflict of Interest

The authors have no conflicts to disclose.

## References

1. Baltz, V.; Manchon, A.; Tsoi, M.; Moriyama, T.; Ono, T.; Tserkovnyak, Y. *Reviews of Modern Physics* **2018,** 90, (1).
2. Smejkal, L.; Sinova, J.; Jungwirth, T. *arXiv* **2021,** 2105.05820.
3. Reichlova, H.; Lopes Seeger, R.; Gonzalez-Hernandez, R.; Kounta, I.; Schlitz, R.; Kriegner, D.; Ritzinger, P.; Lammel, M.; Leiviska, M.; Petricek, V.; Dolezal, P.; Schmoranzerova, E.; ın Badura, A.; Thomas, A.; Baltz, V.; Michez, L.; Sinova, J.; Goennenwein, S. T. B.; Jungwirth, T.; Smejkal, L. *arXiv* **2021,** 2012.15651.
4. Kamra, A.; Wimmer, T.; Huebl, H.; Althammer, M. *Physical Review B* **2020,** 102, (17).
5. Olejnik, K.; Schuler, V.; Marti, X.; Novak, V.; Kaspar, Z.; Wadley, P.; Campion, R. P.; Edmonds, K. W.; Gallagher, B. L.; Garces, J.; Baumgartner, M.; Gambardella, P.; Jungwirth, T. *Nat Commun* **2017,** 8, 15434.
6. Olejník, K.; Seifert, T.; Kašpar, Z.; Novák, V.; Wadley, P.; Campion, R. P.; Baumgartner, M.; Gambardella, P.; Němec, P.; Wunderlich, J.; Sinova, J.; Kužel, P.; Müller, M.; Kampfrath, T.; Jungwirth, T. *Science Advances* **2018,** 4, (3), eaar3566.
7. Wadley, P.; Howells, B.; Železný, J.; Andrews, C.; Hills, V.; Campion, R. P.; Novák, V.; Olejník, K.; Maccherozzi, F.; Dhesi, S. S.; Martin, S. Y.; Wagner, T.; Wunderlich, J.; Freimuth, F.; Mokrousov, Y.; Kuneš, J.; Chauhan, J. S.; Grzybowski, M. J.; Rushforth, A. W.; Edmonds, K. W.; Gallagher, B. L.; Jungwirth, T. *Science* **2016,** 351, (6273), 587.
8. Meinert, M.; Graulich, D.; Matalla-Wagner, T. *Physical Review Applied* **2018,** 9, (6).
9. Bodnar, S. Y.; Smejkal, L.; Turek, I.; Jungwirth, T.; Gomonay, O.; Sinova, J.; Sapozhnik, A. A.; Elmers, H. J.; Klaui, M.; Jourdan, M. *Nat Commun* **2018,** 9, (1), 348.
10. Cheng, R.; Daniels, M. W.; Zhu, J. G.; Xiao, D. *Sci Rep* **2016,** 6, 24223.
11. Fix, M.; Schneider, R.; Michaelis de Vasconcellos, S.; Bratschitsch, R.; Albrecht, M. *Applied Physics Letters* **2020,** 117, (13).
12. Sasaki, Y.; Li, G.; Moriyama, T.; Ono, T.; Mikhaylovskiy, R. V.; Kimel, A. V.; Mizukami, S. *Applied Physics Letters* **2020,** 117, (19).
13. Acharyya, R.; Nguyen, H. Y. T.; Pratt, W. P.; Bass, J. *Journal of Applied Physics* **2011,** 109, (7).
14. Zhang, W.; Jungfleisch, M. B.; Jiang, W.; Pearson, J. E.; Hoffmann, A.; Freimuth, F.; Mokrousov, Y. *Phys Rev Lett* **2014,** 113, (19), 196602.
15. van den Brink, A.; Vermijs, G.; Solignac, A.; Koo, J.; Kohlhepp, J. T.; Swagten, H. J. M.; Koopmans, B. *Nat Commun* **2016,** 7, 10854.
16. Oh, Y. W.; Chris Baek, S. H.; Kim, Y. M.; Lee, H. Y.; Lee, K. D.; Yang, C. G.; Park, E. S.; Lee, K. S.; Kim, K. W.; Go, G.; Jeong, J. R.; Min, B. C.; Lee, H. W.; Lee, K. J.; Park, B. G. *Nat Nanotechnol* **2016,** 11, (10), 878-884.

17. Frangou, L.; Oyarzun, S.; Auffret, S.; Vila, L.; Gambarelli, S.; Baltz, V. *Phys Rev Lett* **2016,** 116, (7), 077203.
18. Saglam, H.; Zhang, W.; Jungfleisch, M. B.; Sklenar, J.; Pearson, J. E.; Ketterson, J. B.; Hoffmann, A. *Physical Review B* **2016,** 94, (14).
19. Gladii, O.; Frangou, L.; Forestier, G.; Seeger, R. L.; Auffret, S.; Joumard, I.; Rubio-Roy, M.; Gambarelli, S.; Baltz, V. *Physical Review B* **2018,** 98, (9).
20. Wu, D.; Yu, G.; Chen, C.-T.; Razavi, S. A.; Shao, Q.; Li, X.; Zhao, B.; Wong, K. L.; He, C.; Zhang, Z.; Khalili Amiri, P.; Wang, K. L. *Applied Physics Letters* **2016,** 109, (22).
21. Tshitoyan, V.; Ciccarelli, C.; Mihai, A. P.; Ali, M.; Irvine, A. C.; Moore, T. A.; Jungwirth, T.; Ferguson, A. J. *Physical Review B* **2015,** 92, (21).
22. Qian, L.; Chen, W.; Wang, K.; Wu, X.; Xiao, G. *AIP Advances* **2018,** 8, (11).
23. Chen, M.; Mishra, R.; Wu, Y.; Lee, K.; Yang, H. *Advanced Optical Materials* **2018,** 6, (17).
24. Vaidya, P.; Morley, S. A.; Tol, J. v.; Liu, Y.; Cheng, R.; Brataas, A.; Lederman, D.; Barco, E. d. *Science* **2020,** 368, (6487), 160-165.
25. Li, J.; Wilson, C. B.; Cheng, R.; Lohmann, M.; Kavand, M.; Yuan, W.; Aldosary, M.; Agladze, N.; Wei, P.; Sherwin, M. S.; Shi, J. *Nature* **2020,** 578, (7793), 70-74.
26. Qiu, H.; Zhou, L.; Zhang, C.; Wu, J.; Tian, Y.; Cheng, S.; Mi, S.; Zhao, H.; Zhang, Q.; Wu, D.; Jin, B.; Chen, J.; Wu, P. *Nature Physics* **2020,** 17, (3), 388-394.
27. Gladii, O.; Frangou, L.; Hallal, A.; Seeger, R. L.; Noël, P.; Forestier, G.; Auffret, S.; Rubio-Roy, M.; Warin, P.; Vila, L.; Wimmer, S.; Ebert, H.; Gambarelli, S.; Chshiev, M.; Baltz, V. *Physical Review B* **2019,** 100, (17).
28. Seifert, T.; Jaiswal, S.; Martens, U.; Hannegan, J.; Braun, L.; Maldonado, P.; Freimuth, F.; Kronenberg, A.; Henrizi, J.; Radu, I.; Beaurepaire, E.; Mokrousov, Y.; Oppeneer, P. M.; Jourdan, M.; Jakob, G.; Turchinovich, D.; Hayden, L. M.; Wolf, M.; Münzenberg, M.; Kläui, M.; Kampfrath, T. *Nature Photonics* **2016,** 10, (7), 483-488.
29. Seifert, T. S.; Tran, N. M.; Gueckstock, O.; Rouzegar, S. M.; Nadvornik, L.; Jaiswal, S.; Jakob, G.; Temnov, V. V.; Münzenberg, M.; Wolf, M.; Kläui, M.; Kampfrath, T. *Journal of Physics D: Applied Physics* **2018,** 51, (36), 364003.
30. Rouzegar, R.; Brandt, L.; Nadvornik, L.; Reiss, D. A.; Chekhov, A. L.; Gueckstock, O.; In, C.; Wolf, M.; Seifert, T. S.; Brouwer, P. W.; Woltersdorf, G.; Kampfrath, T. *arXiv* **2021,** 2103.11710.
31. Leitenstorfer, A.; Hunsche, S.; Shah, J.; Nuss, M. C.; Knox, W. H. *Applied Physics Letters* **1999,** 74, (11), 1516-1518.
32. Kampfrath, T.; Nötzold, J.; Wolf, M. *Applied Physics Letters* **2007,** 90, (23).
33. Ingvarsson, S.; Ritchie, L.; Liu, X. Y.; Xiao, G.; Slonczewski, J. C.; Trouilloud, P. L.; Koch, R. H. *Physical Review B* **2002,** 66, (21).
34. Azzawi, S.; Hindmarch, A. T.; Atkinson, D. *Journal of Physics D: Applied Physics* **2017,** 50, (47).
35. Gueckstock, O.; Nadvornik, L.; Gradhand, M.; Seifert, T. S.; Bierhance, G.; Rouzegar, R.; Wolf, M.; Vafaee, M.; Cramer, J.; Syskaki, M. A.; Woltersdorf, G.; Mertig, I.; Jakob, G.; Klaui, M.; Kampfrath, T. *Adv Mater* **2021,** 33, (9), e2006281.
36. Sinova, J.; Valenzuela, S. O.; Wunderlich, J.; Back, C. H.; Jungwirth, T. *Reviews of Modern Physics* **2015,** 87, (4), 1213-1260.
37. Zhang, W.; Jungfleisch, M. B.; Jiang, W.; Sklenar, J.; Fradin, F. Y.; Pearson, J. E.; Ketterson, J. B.; Hoffmann, A. *Journal of Applied Physics* **2015,** 117, (17).
38. Amin, V. P.; Stiles, M. D. *Physical Review B* **2016,** 94, (10).
39. Wahada, M. A.; Sasioglu, E.; Hoppe, W.; Zhou, X.; Deniz, H.; Rouzegar, R.; Kampfrath, T.; Mertig, I.; Parkin, S. S. P.; Woltersdorf, G. *arXiv* **2021,** 2108.01770.
40. Seifert, T. S.; Martens, U.; Radu, F.; Ribow, M.; Berritta, M.; Nadvornik, L.; Starke, R.; Jungwirth, T.; Wolf, M.; Radu, I.; Munzenberg, M.; Oppeneer, P. M.; Woltersdorf, G.; Kampfrath, T. *Adv Mater* **2021,** 33, (14), e2007398.
41. Nádvorník, L.; Borchert, M.; Brandt, L.; Schlitz, R.; de Mare, K. A.; Výborný, K.; Mertig, I.; Jakob, G.; Kläui, M.; Goennenwein, S. T. B.; Wolf, M.; Woltersdorf, G.; Kampfrath, T. *Physical Review X* **2021,** 11, (2).
42. Zhu, Y.-H.; Hillebrands, B.; Schneider, H. C. *Physical Review B* **2009,** 79, (21).
43. Seifert, T. S.; Jaiswal, S.; Barker, J.; Weber, S. T.; Razdolski, I.; Cramer, J.; Gueckstock, O.; Maehrlein, S. F.; Nadvornik, L.; Watanabe, S.; Ciccarelli, C.; Melnikov, A.; Jakob, G.; Munzenberg, M.;

Goennenwein, S. T. B.; Woltersdorf, G.; Rethfeld, B.; Brouwer, P. W.; Wolf, M.; Klaui, M.; Kampfrath, T. *Nat Commun* **2018,** 9, (1), 2899.
44. Jiménez-Cavero, P.; Gueckstock, O.; Nádvorník, L.; Lucas, I.; Seifert, T. S.; Wolf, M.; Rouzegar, R.; Brouwer, P. W.; Becker, S.; Jakob, G.; Kläui, M.; Guo, C.; Wan, C.; Han, X.; Jin, Z.; Zhao, H.; Wu, D.; Morellón, L.; Kampfrath, T. *arXiv:2110.05462* **2021**.
45. Merodio, P.; Ghosh, A.; Lemonias, C.; Gautier, E.; Ebels, U.; Chshiev, M.; Béa, H.; Baltz, V.; Bailey, W. E. *Applied Physics Letters* **2014,** 104, (3).
46. Beaurepaire, E.; Turner, G. M.; Harrel, S. M.; Beard, M. C.; Bigot, J. Y.; Schmuttenmaer, C. A. *Applied Physics Letters* **2004,** 84, (18), 3465-3467.
47. Zhang, W.; Maldonado, P.; Jin, Z.; Seifert, T. S.; Arabski, J.; Schmerber, G.; Beaurepaire, E.; Bonn, M.; Kampfrath, T.; Oppeneer, P. M.; Turchinovich, D. *Nat Commun* **2020,** 11, (1), 4247.
48. Zhou, C.; Liu, Y. P.; Wang, Z.; Ma, S. J.; Jia, M. W.; Wu, R. Q.; Zhou, L.; Zhang, W.; Liu, M. K.; Wu, Y. Z.; Qi, J. *Phys Rev Lett* **2018,** 121, (8), 086801.
49. Dang, T. H.; Barbedienne, Q.; To, D. Q.; Rongione, E.; Reyren, N.; Godel, F.; Collin, S.; George, J. M.; Jaffrès, H. *Physical Review B* **2020,** 102, (14).
50. Dang, T. H.; Hawecker, J.; Rongione, E.; Baez Flores, G.; To, D. Q.; Rojas-Sanchez, J. C.; Nong, H.; Mangeney, J.; Tignon, J.; Godel, F.; Collin, S.; Seneor, P.; Bibes, M.; Fert, A.; Anane, M.; George, J. M.; Vila, L.; Cosset-Cheneau, M.; Dolfi, D.; Lebrun, R.; Bortolotti, P.; Belashchenko, K.; Dhillon, S.; Jaffrès, H. *Applied Physics Reviews* **2020,** 7, (4).

# Supplementary Material

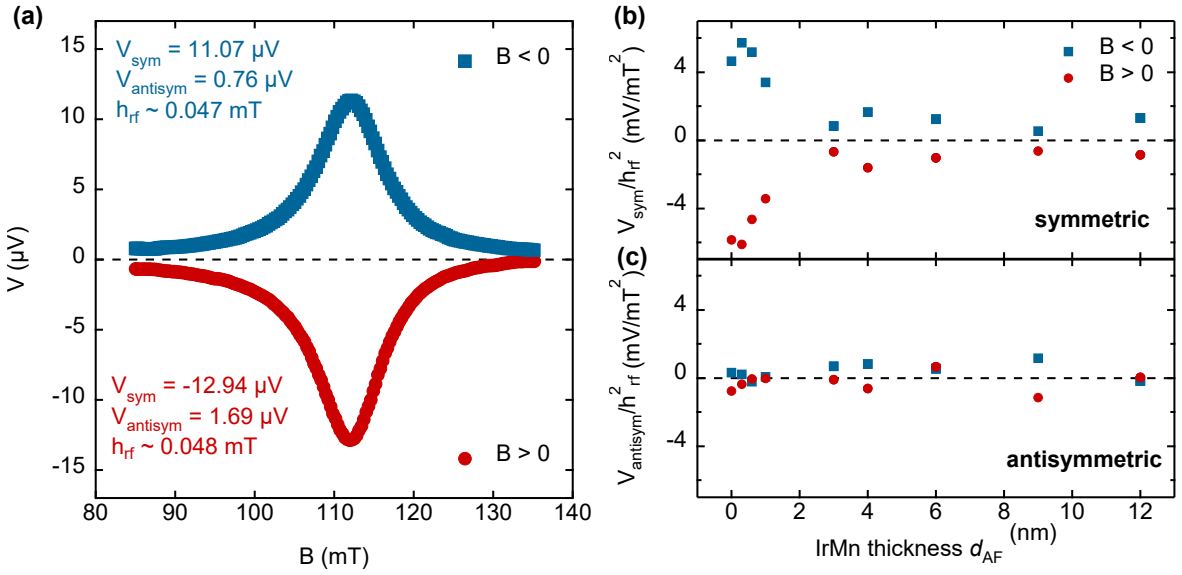


**FIG. S1. | Data treatment to extract the S2C signal from raw data in the GHz experiments. (a)** Representative data showing $B$-dependence of raw voltage $V$, as measured for a Pt|IrMn|NiFe sample, for $B > 0$ and $B < 0$. An input power $P = 40\,\mathrm{mW}$ was used, corresponding to an excitation magnetic field of $h_{\mathrm{rf}}$. The precise value of this field was determined for each sample by measuring the quality factor of the 3 loop – 2 gap resonator $Q$ and using the equation given for our MS5 resonator: $\mathrm{h}_{\mathrm{rf}}^2 = 4\mathrm{PQ}/500$. For each sample, those raw voltages vs $B$ were fitted using the following equation: $V = V_{\mathrm{sym}}\left(\Delta B_{pp}\sqrt{3}/2\right)^2/[\left(\Delta B_{pp}\sqrt{3}/2\right)^2 + (B - B_{\mathrm{res}})^2] - V_{\mathrm{antisym}}\left(\Delta B_{pp}\sqrt{3}/2\right)(B - B_{\mathrm{res}})/[\left(\Delta B_{pp}\sqrt{3}/2\right)^2 + (B - B_{\mathrm{res}})^2]$, where $\Delta B_{pp}$ is the the peak-to-peak line width, and $B_{\mathrm{res}}$ is the resonance field. The fit returned the symmetric, $V_{\mathrm{sym}}$, and antisymmetric, $V_{\mathrm{antisym}}$ contributions. **(b)** IrMn thickness-dependence of $V_{\mathrm{sym}}$, and **(c)**, $V_{\mathrm{antisym}}$ normalized by $\mathrm{h}_{\mathrm{rf}}^2$. This normalization accounts for the input power reaching the sample. The S2C signals, shown in Fig. 2, correspond to the average of $I_c = V_{\mathrm{sym}}/\left(Rh_{\mathrm{rf}}^2\right)$ for $B > 0$ and $B < 0$., where $R$ is the resistance of the stack, experimentally measured.

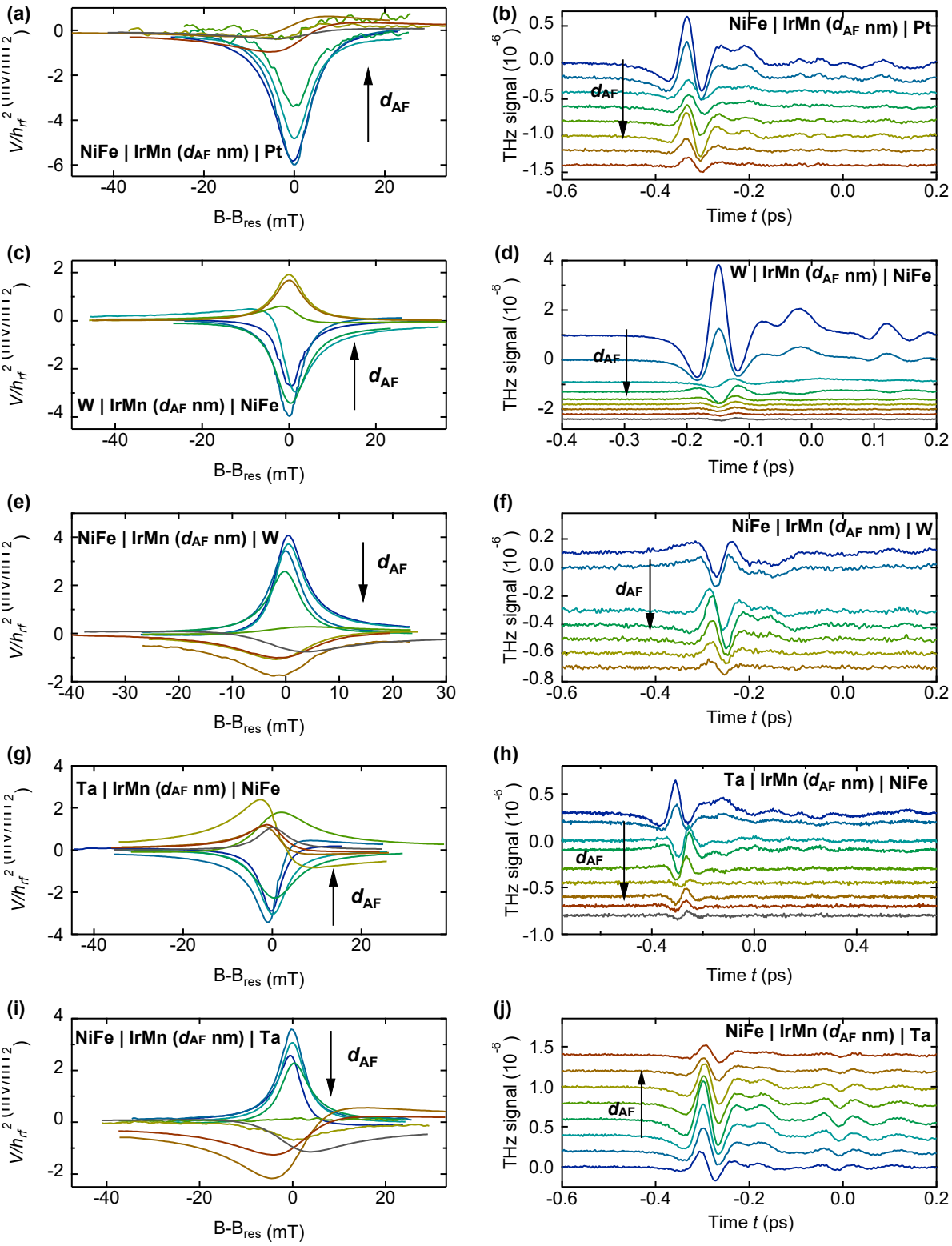


**FIG. S2. | Raw data from GHz and THz experiments.**

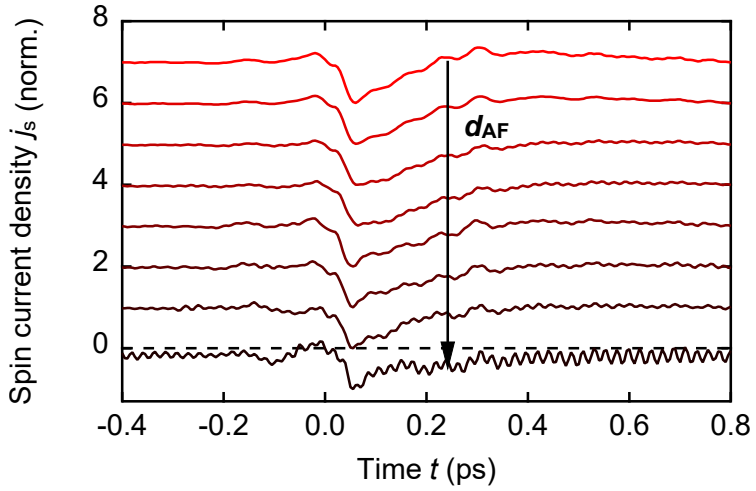


**FIG. S3. | Spin currents for different IrMn thicknesses.** Extracted pin current densities $j_s(t, d_{AF})$ from Pt|IrMn($d_{AF}$ nm)|NiFe normalized to $j_s(t, d_{AF} = 0)$. The arrow depicts the increasing thickness $d_{AF}$ of the IrMn layer ranging from 0 nm to 12 nm. All $j_s(t, d)$ exhibit the same ultrafast temporal dynamics indicating that the origin of the spin currents $j_s(t, d_{AF})$ is the same for all thicknesses $d_{AF}$ of IrMn.

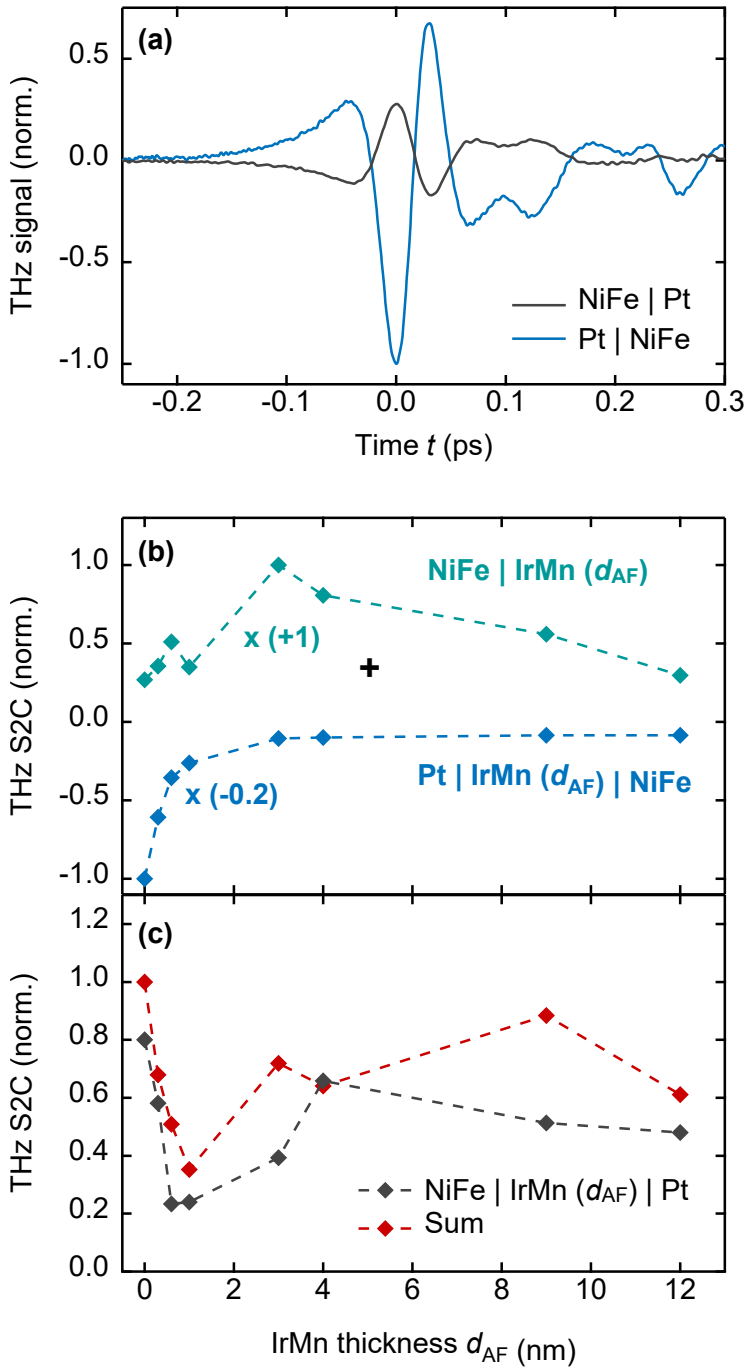


**FIG. S4. | Interfacial contributions to the THz signal. (a)** Comparison of the emitted THz waveform from forward- and reversed-grown stacks of Pt|NiFe (blue curve) and NiFe|Pt (grey curve). **(b, c)** By superposing and rescaling the signals of Pt|IrMn|NiFe and NiFe|IrMn as shown in panel (b), it is possible to reconstruct the trend of NiFe|IrMn|Pt [panel (c) and Fig. 2(d)]. This indicates that the interface quality between NiFe and IrMn can be drastically influenced by the stacking order of the layers.

| | N | $y_{0,\mathrm{THz}}$ | $y_{1,\mathrm{THz}}$ | $y_{0,\mathrm{GHz}}$ | $y_{1,\mathrm{GHz}}$ |
|---|---|---|---|---|---|
| **N \| IrMn \| NiFe (forward-grown)** | Pt | -0.09 ± 0.01 | -0.9 ± 0.02 | -0.06 ± 0.03 | -1.04 ± 0.08 |
| | W | -0.10 ± 0.01 | 1.02 ± 0.07 | -0.19 ± 0.06 | 1.27 ± 0.01 |
| | Ta | -0.08 ± 0.02 | 0.38 ± 0.07 | -0.23 ± 0.05 | 0.81 ± 0.07 |
| **NiFe \| IrMn \| N (reversely grown)** | Pt | – | – | 0.08 ± 0.03 | 0.64 ± 0.09 |
| | W | 0.12 ± 0.02 | -0.22 ± 0.16 | 0.20 ± 0.02 | -0.63 ± 0.04 |
| | Ta | 0.19 ± 0.04 | -0.13 ± 0.07 | 0.13 ± 0.06 | -0.55 ± 0.06 |

**TABLE S1. | Fitting parameters $y_0$ and $y_1$ of the spin current in Fig. 2.** Fits are mono-exponential functions specified in the main text. The errors are obtained from fitting statistics and repeated experiments.